Catalysis Today 139 (2008) 29–36

Contents lists available at ScienceDirect

Catalysis Today

journal homepage: www.elsevier.com/locate/cattod

$AuO_x/Ce_{0.6}Zr_{0.3}Y_{0.1}O_2$ nano-sized catalysts active for the oxidation of methane

Yujuan Zhang, Jiguang Deng, Lei Zhang, Wenge Qiu, Hongxing Dai *, Hong He

Laboratory of Catalysis Chemistry and Nanoscience, Department of Chemistry and Chemical Engineering, College of Environmental and Energy Engineering, Beijing University of Technology, Beijing 100124, China

ARTICLE INFO

Article history:
Available online 11 September 2008

Keywords:
Ceria–zirconia–yttria solid solution
Supported gold catalyst
Methane combustion
In situ reduction method

ABSTRACT

The nano-sized polycrystalline $Ce_{0.6}Zr_{0.3}Y_{0.1}O_2$ (CZY) support was fabricated adopting the cetyltrimethyl ammonium bromide (CTAB)-assisted hydrothermal treatment method and the CZY-supported nano-sized gold catalysts, *y*% AuO_x/CZY (*y*% represents the Au weight percentage, $y = 0.2–10.0$), were prepared using an *in situ* reduction procedure with $HAuCl_4$ as Au source, $NaBH_4$ as reducing agent, and poly(*N*-vinyl-2-pyrrolidone) (PVP) as surfactant. We characterized the physicochemical properties of these materials by means of the XRD, Brunauer-Emmett-Teller (BET), high-resolution scanning electron microscopic (HRSEM), high-resolution transmission electron microscopic (HRTEM)/selected area electron diffraction (SAED), XPS, and hydrogen temperature-programmed reduction (H_2-TPR) techniques, and examined their catalytic activities for the combustion of methane. It is observed that the CZY and gold were nanoparticles with the diameter of 5–50 and 2–20 nm, respectively. At a lower gold loading ($y \leq 0.6$), the gold mainly existed in a highly dispersed AuO_x (Au^{3+}) domain on the CZY surfaces; at a higher gold loading ($y \geq 1.0$), the gold were present in the form of metallic Au^0 cluster as well as dispersed AuO_x domains. With the introduction of gold, the reducibility of the *y*% AuO_x/CZY catalysts was improved significantly, possibly due to the synergistic action between the nano-sized gold and the nanocrystalline CZY. Among the *y*% AuO_x/CZY catalysts, the one at $y = 0.2$ showed the best activity for methane combustion. It is suggested that the good catalytic performance of CZY-supported gold materials with a lower gold loading (<1.0%) is associated with the high dispersion of AuO_x domains, high atomic ratio of Au^{3+}/Au^0, nano-sized Au and CZY particles, and good reducibility.

1. Introduction

Combustion of hydrocarbons, especially methane, the main component of natural gas, requires high temperatures, leading to undesired NO_x formation. Catalytic combustion of methane is an effective pathway for the utilization of natural gas because it can take place at lower temperatures, thus reducing the emission of NO_x significantly. Many materials, such as noble metals, single transition metal oxides and their binary oxides, and mixed metal oxides with a perovsike- or spinel-type structure have been tested as catalyst for the combustion of methane. Among which supported PdO has been thought to perform the best [1]. In recent years, however, the unusual catalytic activity of TiO_2-loaded nano-sized gold in CO oxidation at room temperature (RT) [2] renews the interest of this less precious metal in the application of oxidation catalysis.

Gold-based catalysts attract less interest for CH_4 oxidation probably due to the need of a high temperature to activate its strong C–H bonds. Waters et al. [3] examined the effect of support on the catalytic performance of co-precipitated Au (loading = 5 - mol%) catalysts for the oxidation of CH_4, and observed an activity order of $Au/Co_3O_4 > Au/NiO_x > Au/MnO_x > Au/Fe_2O_3 \gg Au/CeO_x$. The authors believed that the presence of oxidized Au species in the catalyst contributed to the enhancement in activity. Similar conclusions have also been drawn by other researchers [4–6]. Moreover, the real catalytic sites might be the ensembles containing ionic and metallic gold [7,8]. In addition to the influence of oxidation states of gold, particle size of gold as well as support has also an important effect on the performance of supported gold catalysts. For example, when particle size of the support (e.g. ZrO_2 [9] and CeO_2 [10,11]) matches that of gold nanoparticles, a significant enhancement in catalytic activity could be achieved.

It is known that ceria–zirconia–yttria solid solution (i) possesses a high oxygen vacancy density which is favorable for the complete oxidation of hydrocarbons, and (ii) exhibits a good ability of oxygen storage/release which facilitates the redox process of the catalyst [12]. Such ceria–zirconia-based materials also show moderate catalytic activity for methane combustion [13]. By combining the characteristics of nanometer Au and nano-

* Corresponding author. Tel.: +86 10 6739 6588; fax: +86 10 6739 1983.
E-mail address: hxdai@bjut.edu.cn (H. Dai).

0920-5861/$ – see front matter © 2008 Elsevier B.V. All rights reserved.
doi:10.1016/j.cattod.2008.08.005

sized ceria–zirconia–yttria solid solution, we recently generated a series of nanostructured $Ce_{0.6}Zr_{0.3}Y_{0.1}O_2$ (CZY)-supported nano-sized gold (i.e. AuO_x/CZY) via an *in situ* reduction pathway, and examined their activities in catalyzing methane oxidation. In this work, we report the preparation, characterization, and catalytic properties of the AuO_x/CZY nanomaterials for the addressed reaction.

2. Experimental

2.1. Catalyst preparation

The nano-sized CZY support was fabricated by adopting the cetyltrimethyl ammonium bromide (CTAB)-assisted hydrothermal treatment method described elsewhere [14]. Stoichiometric amounts of $Ce(NO_3)_3{\cdot}6H_2O$, $ZrO(NO_3)_2{\cdot}2H_2O$, $Y(NO_3)_3{\cdot}6H_2O$, and CTAB ((Ce+Zr+Y)/CTAB molar ratio = 1/1.25) were dissolved in deionized water. An ammonia (28 wt.%) solution was added dropwise to the above mixture under stirring and the pH value was carefully regulated to 11 for the generation of yellowish co-precipitates. After being in turn filtered, washed with deionized water and methanol for three times, and dried at 60 °C for 24 h, the co-precipitates were calcined in air from RT to 700 °C at a ramp rate of 1 °C min^{-1} and kept at this temperature for 2 h, thus obtaining the CZY support. The *y*% AuO_x/CZY (*y*% represents the Au weight percentage, *y* = 0.2–10.0) catalysts were prepared by a novel *in situ* reduction method similar to that described elsewhere [15], in which a desired amount of CZY was first put into a mixed solution of $HAuCl_4$ (0.1 mol L^{-1}) and poly(*N*-vinyl-2-pyrrolidone) (PVP) with the PVP/$HAuCl_4{\cdot}4H_2O$ molar ratio = 1/4.86 under ultrasound irradiation and mechanical stirring, then a certain amount of reducer $NaBH_4$ (0.1 mol L^{-1}) solution ($NaBH_4$/$HAuCl_4{\cdot}4H_2O$ molar ratio = 653.2/1) was added dropwise to the above mixed solution. After reaction at RT for 24 h, the solution containing Au/CZY was in turn filtered, washed with deionized water, and filtered again until no Cl^- and Na^+ ions were detected in the filtered solution. The obtained solid was dried at 100 °C overnight and calcined in an oxygen flow of 30 mL min^{-1} from RT to 700 °C at a heating rate of 1 °C min^{-1} and kept at this temperature for 2 h. All the chemicals were analytical pure (Beijing Chemical Reagent Co.) and used without further purification.

2.2. Catalyst characterization

The crystal phase and pore structures of the samples were determined on an X-ray diffractometer (XRD, Bruker/AXS D8 Advance) operating at 40 kV and 200 mA using Cu Kα irradiation and nickel filter (λ = 0.15406 nm). The XRD patterns were recorded in the 2θ range of 0.6−10° for small-angle profiles and 10–80° for wide-angle profiles. Surface areas and pore size distributions as well as N_2 adsorption–desorption isotherms of the samples were measured via N_2 adsorption at −196 °C on a Micromeritics ASAP 2020 apparatus with all samples outgassed at 250 °C for 2 h under vacuum before measurement; surface areas and pore size distributions were calculated according to the Brunauer-Emmett-Teller (BET) and Barrett-Joyner-Halenda (BJH) method, respectively. The high-resolution scanning electron microscopic (HRSEM) images of the samples were recorded on a JEOL JSM 6500F apparatus operating at 10 kV. Before being transferred into the high-resolution scanning electron microscopic chamber, the sample ultrasound-dispersed in ethanol was allowed to settle and dry on a holder. By means of a JEOL-2010 instrument (operating at 200 kV), high-resolution transmission electron microscopic (HRTEM) images and selected area electron diffraction (SAED) patterns of the samples were obtained.

X-ray photoelectron spectroscopy (XPS, VG CLAM 4 MCD analyzer) was employed to determine the O 1s, Au 4f, Ce 3d, Zr 3d, Y 3d, and C 1s binding energies (BEs) of surface species with Mg Kα (*hν* = 1253.6 eV) as the excitation source. The instrumental resolution was 0.5 eV. Before XPS determination, the samples were calcined in O_2 (flow rate, 20 mL min^{-1}) at 500 °C for 1 h for the removal of surface carbonate and adsorbed water. After being cooled to RT in the same atmosphere and purged in helium (flow rate, 40 mL min^{-1}), the samples were in turn transferred to the holder under the protection of helium in a transparent GLOVE BAG (Instruments for Research and Industry, USA), mounted to the spectrometer, outgassed in the preparation chamber (10^{-5} Torr) for 0.5 h, and introduced into the analysis chamber (3×10^{-9} Torr) for recording. The C 1s peak at 284.6 eV was taken as a reference for BE calibration.

Hydrogen temperature-programmed reduction (H_2-TPR) experiments were conducted with a sample (200 mg) first pretreated *in situ* in O_2 (flow rate = 40 mL min^{-1}) at 500 °C for 1 h in a quartz fixed-bed micro-reactor (i.d. = 6 mm). After cooling to RT in the same atmosphere, the sample was exposed to a flow (50 mL min^{-1}) of 5% H_2–95% He (v/v) and heated at a rate of 10 °C min^{-1} to 900 °C. The outlet gases were analyzed on-line over a mass spectrometer (MS) apparatus (Hiden HPR20). The MS response was calibrated against that of the complete reduction of a known standard of powder CuO (Aldrich, 99.995%).

2.3. Catalytic evaluation

Catalytic activity was evaluated in a quartz fixed-bed micro-reactor (i.d. = 8 mm) at atmospheric pressure. 0.12 mL of the catalyst (40–60 mesh) was diluted with an equal amount of quartz sand (40–60 mesh) to eliminate the hot spots within the catalyst bed possibly existing during methane combustion. The reactant mixture was composed of 5% CH_4/95% He (v/v, 40 mL min^{-1}) + O_2 (8 mL min^{-1}) + He (52 mL min^{-1}). The CH_4/O_2 molar ratio and space velocity was 1/4 and 50,000 h^{-1}, respectively. The outlet gases were on-line analyzed by a gas chromatograph (GC, Shimadzu GC-14C), with a 5A molecular sieve column, TCD detector, and helium carrier gas.

3. Results and discussion

3.1. Crystal phase compositions, structures, and textural properties

Fig. 1A shows the wide-angle XRD patterns of the CZY and *y*% AuO_x/CZY samples. It is observed that the XRD pattern of the as-fabricated CZY sample was rather similar to that of cubic $Ce_{0.6}Zr_{0.4}O_2$ (JCPDS PDF# 38-1439), indicating the formation of single-phase cubic crystal structure of CZY [12,14]; these well-resolved peaks can be indexed as shown in Fig. 1A. With the loading of gold, no significant changes in XRD pattern were detected, demonstrating the retention of the cubic CZY structure; when the gold loading was ≥1.0% (Fig. 1A(d–g)), however, two weak diffraction signals at 2θ = 38.5° and 45.0° due to the (1 1 1) and (2 0 0) reflections of Au (JCPDS PDF# 02-1095) were detected, respectively, indicating the formation of metallic gold phase [15–17]. These results suggest that the AuO_x domains were highly dispersed on the CZY surfaces at an Au loading <1.0%. The representative small-angle XRD patterns of CZY and 0.2% AuO_x/CZY samples are shown in Fig. 1B. There was appearance of a weak XRD peak at 2θ = ca. 0.9° in each of the two samples and its peak intensity decreased slightly after the loading of 0.2% Au. Such a weak peak at 2θ = ca. 0.9° is characteristic of mesoporous structures. These mesopores originated from the space of inter-nanoparticles.

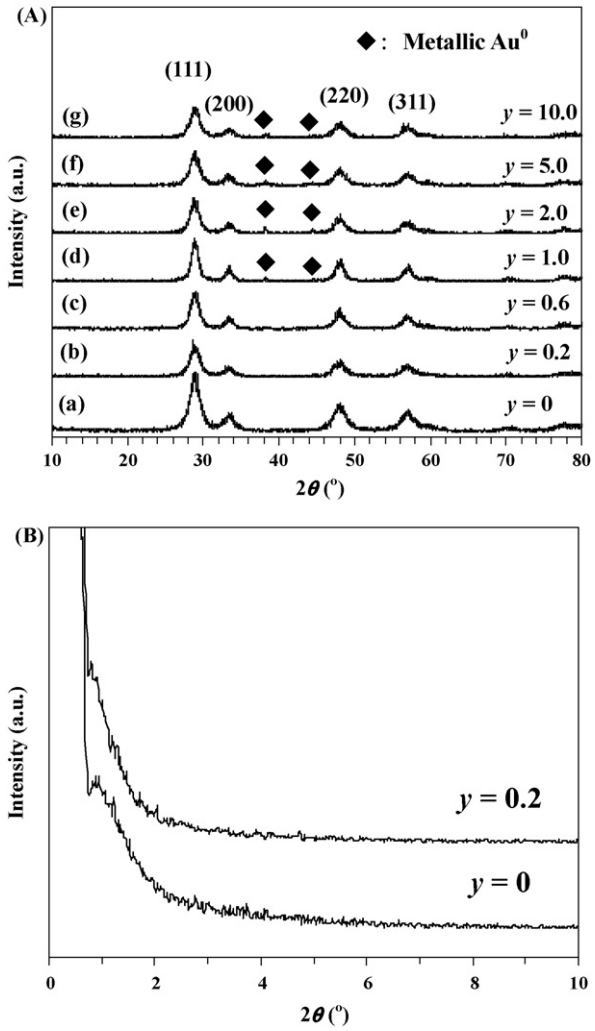

Fig. 1. (A) Wide-angle and (B) small-angle XRD patterns of the *y*% AuO_x/CZY catalysts.

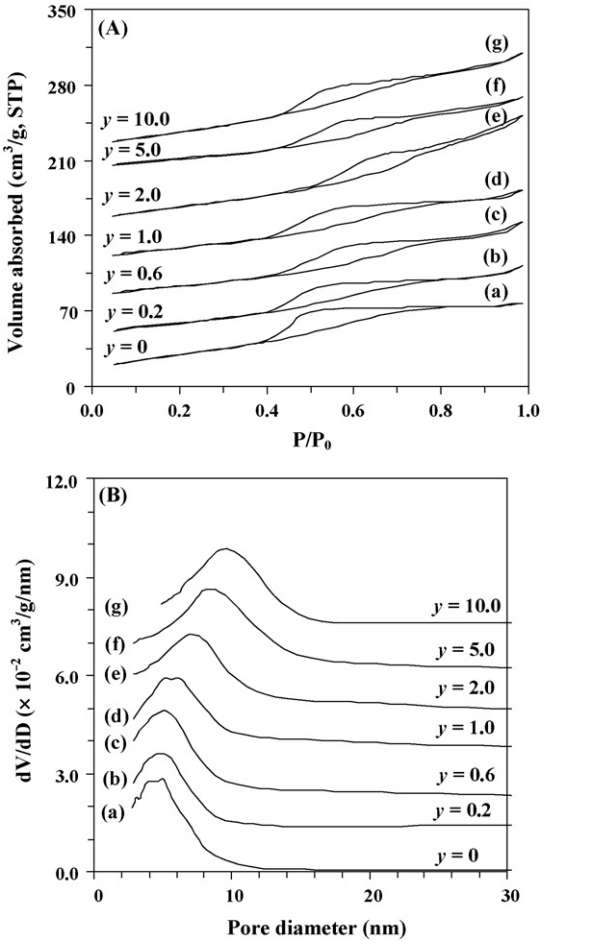

Fig. 2. (A) Nitrogen adsorption–desorption isotherms and (B) pore size distributions of the *y*% AuO_x/CZY catalysts.

Table 1 summarizes the textural parameters of the CZY and *y*% AuO_x/CZY samples. The BET surface area of CZY obtained after calcination at 700 °C for 2 h was 90 $m^2\ g^{-1}$, those of *y*% AuO_x/CZY were in the range of 60–88 $m^2\ g^{-1}$. With the loading of gold, the average pore size increased monotonously but the extent of rise in pore volume changed depending upon the AuO_x loading. Shown in Fig. 2 are the N_2 sorption isotherms and pore size distributions of the CZY and *y*% AuO_x/CZY samples. It is observed from Fig. 2A that the isotherms in the p/p_0 range of 0.4–0.8 were type IV and they were due to the adsorption–desorption of N_2 in the mesopores of interparticles; for the *y*% AuO_x/CZY samples at $y \geq 0.6$, there was also a rather small H_3-type hysteresis loop in the p/p_0 range of 0.8–1.0, attributable to the macropores of interparticles [18]. As seen in Fig. 2B, there was presence of broadening in pore size distribution and an increase in pore size with the loading of gold. It might be a result of the growing of Au particles at elevated gold loading. Furthermore, the average pore diameter estimated from Fig. 2B was 4.5, 4.6, 5.1, 5.6, 7.1, 8.2, and 9.1 nm for the *y*% AuO_x/CZY sample at $y = 0$, 0.2, 0.6, 1.0, 2.0, 5.0, and 10.0, respectively, in good agreement with the results in Table 1.

Table 1
Textural properties of the *y*% AuO_x/CZY catalysts

y (%)	Surface area ($m^2\ g^{-1}$)	Average pore diameter (nm)	Pore volume ($cm^3\ g^{-1}$)
0	90	4.4	0.11
0.2	88	5.0	0.12
0.6	75	5.8	0.17
1.0	74	6.3	0.13
2.0	75	7.6	0.17
5.0	65	8.8	0.12
10.0	60	9.5	0.15

3.2. Surface morphologies

Fig. 3 shows the HRSEM and HRTEM images as well as the SAED patterns of CZY and *y*% AuO_x/CZY. The CZY sample displayed an irregular cluster morphology, each cluster was composed of a number of uniform spherical CZY particles (diameter = 5–10 nm) (Fig. 3A). There were a large number of mesopores between these uniform CZY particles (Fig. 3B). The appearance of multiple bright diffraction rings in the SAED pattern (Fig. 3C) reveals that the as-fabricated CZY material was polycrystalline. The recording of well-resolved lattice fringes (Fig. 3C) indicates the generation of a well-grown CZY solid solution, the *d* spacing (0.31 nm) was quite similar to that of cubic $Ce_{0.6}Zr_{0.4}O_2$ (JCPDS PDF# 38-1439). Compared to the CZY sample, the 2.0% AuO_x/CZY one showed an increase in particle size of CZY (diameter = 5–50 nm) but no significant change in morphology of the CZY particles was observed (Fig. 3D); there was detection of a number of Au particles with a diameter of 2–8 nm dispersed throughout the CZY sample

(Fig. 3E); the polycrystalline structure of CZY still retained as evidenced by the several bright diffraction rings in the SAED pattern (inset of Fig. 3F), and the *d* spacing was estimated to be 0.31 nm for the (1 1 1) plane of CZY (Fig. 3F). With the rise in gold loading to 10.0%, the CZY cluster became much larger (Fig. 3G) although the CZY particle size retained in the range of 5–50 nm (Fig. 3H), there were more quantity of metallic Au^0 detected by the HRTEM technique and part of the Au^0 aggregated into big particles with the diameter being in the range of 6–20 nm (Fig. 3H); the SAED pattern (inset of Fig. 3I) contained some bright spots, somewhat different from those of CZY and 2.0% AuO_x/CZY, indicating that the metallic Au^0 contributed to the alteration of the electron diffraction pattern; the *d* spacing of the CZY (1 1 1) plane of the 10.0% AuO_x/CZY sample did not change in comparison with those of CZY and 2.0% AuO_x/CZY. It is worth pointing out that there was no detection of Au^0 particles by the HRTEM technique in the 0.2% AuO_x/CZY sample, possibly due to the rather low Au^0 loading of this sample.

3.3. Surface Ce and Au oxidation states

Shown in Fig. 4 are the O 1s, Au 4f, and Ce 3d core level XPS spectra. It is seen from Fig. 4A that there was an unsymmetrical peak at BE = ca. 530 eV, which could be decomposed into two components at BE = 529.6 and 530.9 eV, attributable to the surface lattice oxygen and adsorbed oxygen (e.g. O_2^-, O_2^{2-} or O^-) species [19,20] in/on the CZY and *y*% AuO_x/CZY samples, respectively. The presence of surface hydroxyl species could be excluded since the samples were pretreated in O_2 at 500 °C and the recording of their XPS spectra was carried out without exposure to the air. These

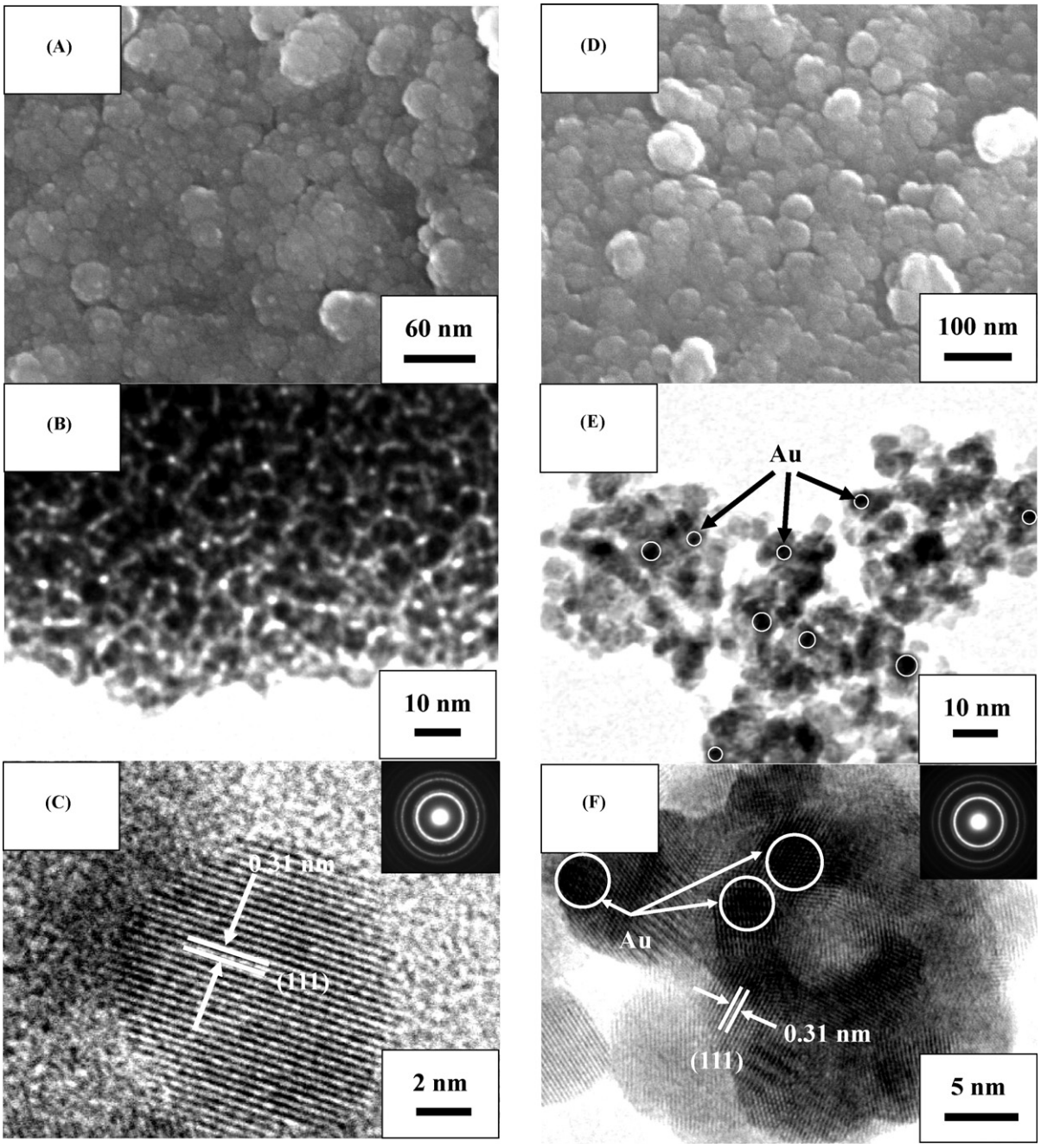

Fig. 3. HRSEM (A, D, G) and HRTEM (B, C, E, F, H, I) images as well as SAED patterns (insets) of (A–C) CZY, (D–F) 2.0% AuO_x/CZY, and (G–I) 10.0% AuO_x/CZY.

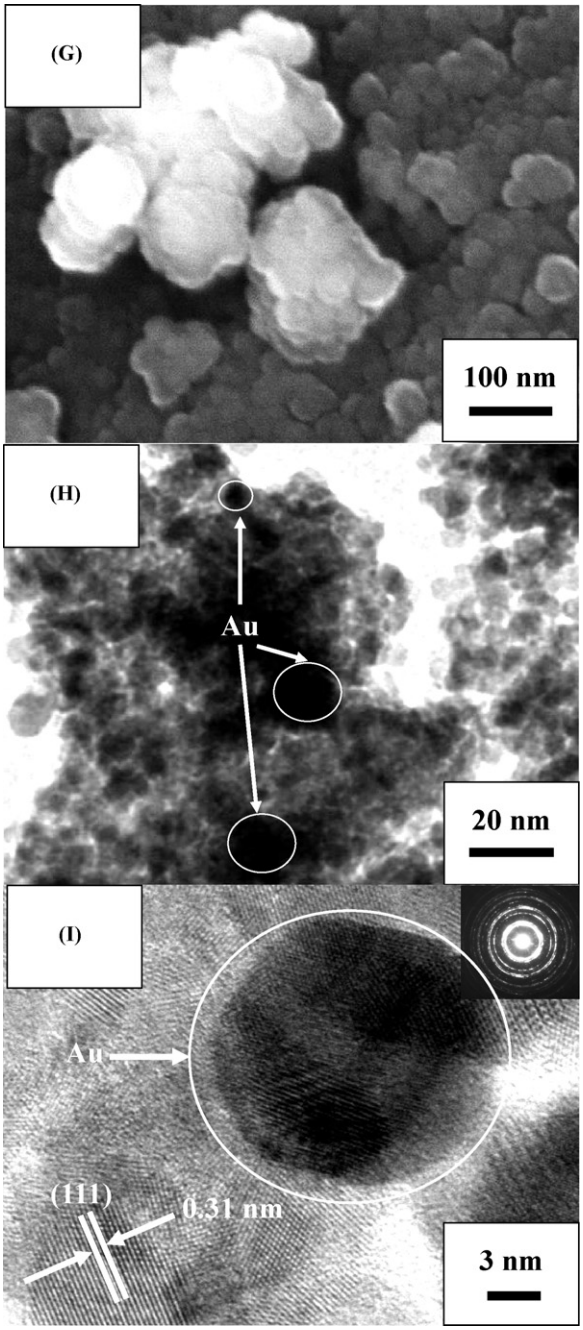

Fig. 3. (*Continued*).

oxygen species mainly originated from the CZY solid solution. It has been reported that there was presence of oxygen vacancies in $Ce_{1-x}Zr_xO_2$ [21–23], and the doping of Y^{3+} ions to the lattice of ceria–zirconia solid solution could further increase the density of oxygen vacancies [12,24]. From Fig. 4B, one can observe that there were two sets of signals: one was at BE = 882.5, 884.7, 889.7, and 898.5 eV attributable to the Ce $3d_{5/2}$; the other was at BE = 901.0, 903.5, 907.8, and 916.6 eV attributable to the Ce $3d_{3/2}$ [25,26]. The signals at BE = 884.7 and 903.5 eV were due to Ce^{3+} whereas the ones at other BEs were due to Ce^{4+} [25,26]. That is to say, the cerium in the CZY and *y*% AuO_x/CZY samples existed in tri- and tetra-valency. The surface Ce^{3+}/Ce^{4+} atomic ratios were estimated according the XPS spectra and shown in Table 2. Based on the principle of electroneutrality, we hence conclude that there was presence of oxygen vacancies in CZY and CZY-supported gold catalysts. Usually, oxygen molecules can be adsorbed at the sites of oxygen vacancies of these materials. Therefore, we believe that the oxygen adspecies should locate at the surface oxygen vacancies of CZY as well as the interface between the gold and the CZY. The $Ce_{1-x}Zr_xO_2$ materials have good oxygen storage/release ability due to the presence of cerium ions with mixed oxidation states [27,28], which would facilitate the redox process of $Ce^{3+} \Leftrightarrow Ce^{4+}$ [12,29]. From Fig. 4C, one can observe that there were two well-resolved unsymmetrical peaks centered at BE = ca. 85 and 89 eV, which could reasonably be decomposed into components at BE = 84.8 and 85.8 eV and at BE = 88.6 and 89.6 eV, respectively. The components at BE = 84.8 and 88.6 eV were characteristic of Au $4f_{7/2}$, whereas the ones at BE = 85.8 and 89.6 eV were characteristic of Au $4f_{5/2}$. According to the XPS results of supported gold reported by other researchers [8,15,30–36], we could assign the signals at BE = 85.8 and 89.6 eV to Au^{3+} while the ones at BE = 84.8 and 88.6 eV to Au^0. The XPS signal intensity of the fresh and used (after 220 min of on-stream reaction) 0.2% AuO_x/CZY samples was weak, due to the low gold loading and high dispersion of AuO_x. Such weak signal intensity would give rise to some uncertainty in estimating the Au^{3+}/Au^0 atomic ratio. By adopting peak decomposition, one can realize that there were only Au^{3+} ions in the 0.2% AuO_x/CZY, whereas Au^{3+} and Au^0 coexisted in the *y*% AuO_x/CZY at $y \geq 0.6$. It indicates the appearance of metallic gold at a loading of 0.6% that is lower than that (1.0%) detectable by XRD techniques. This discrepancy is understandable because the XPS analysis is more sensitive than the XRD technique in detecting chemical phases. Furthermore, the surface Au^{3+}/Au^0 atomic ratio decreased with the rise in gold loading (Table 2). These results suggest that at a lower gold loading ($y \leq 0.6$), the gold mainly existed in a highly dispersed AuO_x domain on the surfaces of CZY; above this gold loading, the gold existed in the form of metallic Au^0 cluster as well as dispersed AuO_x domain, with the content of the former augmenting at elevated gold loading.

3.4. Reducibility

The reducibility of the CZY and *y*% AuO_x/CZY samples was determined using the TPR technique, as illustrated in Fig. 5. For the CZY sample, there was a broad and weak reduction band centered at 575 °C (Fig. 5a) due to the removal of surface oxygen adspecies and the reduction of Ce^{4+} to Ce^{3+} [37], the H_2 consumption was 0.83 mmol g_{cat}^{-1}. With the loading of gold, the *y*% AuO_x/CZY (y = 0.2–10.0) samples also showed only one reduction band (Fig. 5(b–g)); the peaked temperature was 210, 235, 224, 225, 223, and 220 °C, respectively, and the corresponding H_2 consumption was 1.42, 1.28, 1.19, 1.01, 1.36, and 1.22 mmol g_{cat}^{-1}. The significant drop in reduction temperature of the CZY sample after gold loading might be a result of the presence of highly dispersed reducible AuO_x domains and of the strong interaction between the metallic gold and the CZY that would promote the reduction of Ce^{4+} to Ce^{3+}. Such a shift in reduction temperature induced by gold loading is in agreement with the results reported in the literature [38]. The enhancement in reducibility of the support upon gold loading has also been previously ascribed to a stronger interaction between the metal and the support [39].

Assuming that the Au^{3+} ions were reduced to Au^0 and all the cerium ions were in tetravalency and reduced to Ce^{3+}, one can calculate the theoretical H_2 consumptions of the *y*% AuO_x/CZY samples, which fell into the range of 1.6–1.7 mmol g_{cat}^{-1} for these samples (Table 2). By quantifying the reduction bands in Fig. 5, however, one can obtain their corresponding experimental H_2 consumptions (Table 2). Obviously, the experimental value was lower than the theoretical one for the same sample, with the 0.2%

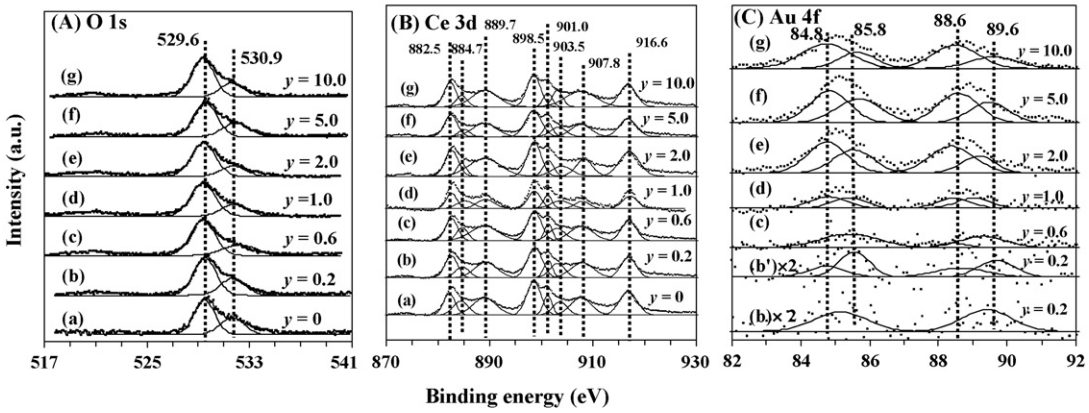

Fig. 4. (A) O 1s, (B) Ce 3d, and (C) Au 4f XPS spectra of the fresh *y*% AuO_x/CZY (a–g) and used 0.2% AuO_x/CZY (b') catalysts.

AuO_x/CZY sample showing the maximal reduction below 400 °C. The presence of Au nanoparticles on the surfaces of cerium-based supports could promote the reduction of surface and near-surface Ce^{4+} ions and inhibit the reduction of the bulk with H_2, possibly due to its poor ability of activating hydrogen molecules [40]. It means that only part of Ce^{4+} ions could be reduced to Ce^{3+} ions. Therefore, it is understandable that the measured H_2 consumption was less than the theoretical one for each of the *y*% AuO_x/CZY sample.

3.5. Catalytic performance

Fig. 6 shows the catalytic performance of *y*% AuO_x/CZY. Apparently, the loading of gold resulted in a significant enhancement in the catalytic activity of CZY. Due to the adopting of efficient *in situ* reduction of $HAuCl_4$ with strong reducer $NaBH_4$, the loss of Au species would be insignificant. That is to say, the nominal Au loading was close to the actual Au amount for each sample. Under the conditions of CH_4/O_2 molar ratio = 1/4 and space velocity = 50,000 h^{-1}, the light-off temperature $T_{50\%}$ (CH_4 conversion = 50%) and complete conversion temperature $T_{100\%}$ were 840 and 870 °C, 600 and 660 °C, 584 and 680 °C, 600 and 720 °C, 620 and 720 °C, 635 and 700 °C, and 680 and 766 °C over *y*% AuO_x/CZY at $y = 0$, 0.2, 0.6, 1.0, 2.0, 5.0 and 10.0, respectively (Fig. 6A). According to the CH_4 conversion at elevated temperatures, it seems that the catalytic activities of *y*% AuO_x/CZY at $y = 0.2$–1.0 were similar and better than those of *y*% AuO_x/CZY at $y \geq 2.0$. For the supported gold catalysts, however, it is more appropriate to compare their catalytic activities by using the methane reaction rate normalized by per gram of gold (i.e. mass specific rate) [30]. Fig. 6B illustrates the reaction rate of CH_4 as a function of reaction temperature. The difference in catalytic performance of these materials thus became rather clear, i.e. the activity of *y*% AuO_x/CZY decreased with the rise in gold loading. The best performance was achieved over the 0.2% AuO_x/CZY catalyst ($T_{100\%}$ = 660 °C at 50,000 h^{-1}). To examine the thermal stability of the 0.2% AuO_x/CZY catalyst, we measured its catalytic activity within 220 min of on-stream reaction and the result is shown in Fig. 7. It is observed that after 190 min of reaction methane conversion started to decrease slowly. This deterioration in catalytic performance might be associated with the change in Au^{3+}/Au^0 atomic ratio, as confirmed by the XPS result (Fig. 4C and Table 2). Xu and co-workers has also reported that the catalyst with a lower gold loading showed a better activity than the one with a higher gold loading, and such an outcome was believed to be associated with the dispersion of Au and the atomic ratio of Au^{3+}/Au^0 [30]. It is well known that for the combustion of hydrocarbons over supported metal catalysts the conversion of a hydrocarbon generally decreases with the rise in space velocity. Due to much higher space velocity adopted in our work than that employed in Nieuwenhuys and co-workers' work, we could reasonably deduce

Table 2
Surface Au^{3+}/Au^0 and Ce^{3+}/Ce^{4+} atomic ratios and theoretical and experimental H_2 consumptions of the *y*% AuO_x/CZY catalysts

y (%)	Surface Au^{3+}/Au^0 atomic ratio[a]	Surface Ce^{3+}/Ce^{4+} atomic ratio[a]	Theoretical H_2 consumption (mmol g_{cat}^{-1})[b]	Experimental H_2 consumption (mmol g_{cat}^{-1})[c]
0	–	0.26	1.58	0.83
0.2	∞ (1.58)[d]	0.21	1.65	1.42
0.6	10.52	0.19	1.67	1.28
1.0	0.91	0.16	1.71	1.19
2.0	0.61	0.17	1.70	1.01
5.0	0.53	0.16	1.74	1.36
10.0	0.33	0.16	1.71	1.22

[a] The data were estimated according to the results of XPS investigations.
[b] The data were obtained according to the reduction of surface Au^{3+} to Au^0 and surface Ce^{4+} to Ce^{3+}.
[c] The data were obtained from the quantification of the H_2-TPR reduction bands.
[d] The datum in parenthesis was estimated from the XPS result of the used (after 220 min of on-stream reaction) 0.2% AuO_x/CZY sample. The uncertainty for the estimation of surface Au^{3+}/Au^0 atomic ratios in the fresh and used 0.2% AuO_x/CZY samples was ±5%.

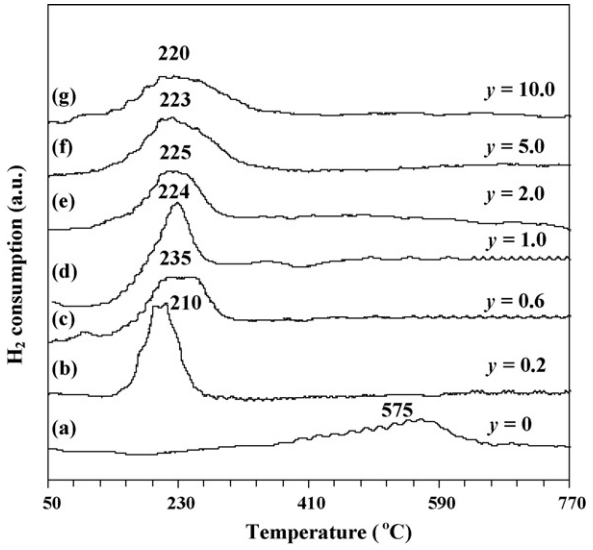

Fig. 5. TPR profiles of the *y*% AuO_x/CZY catalysts.

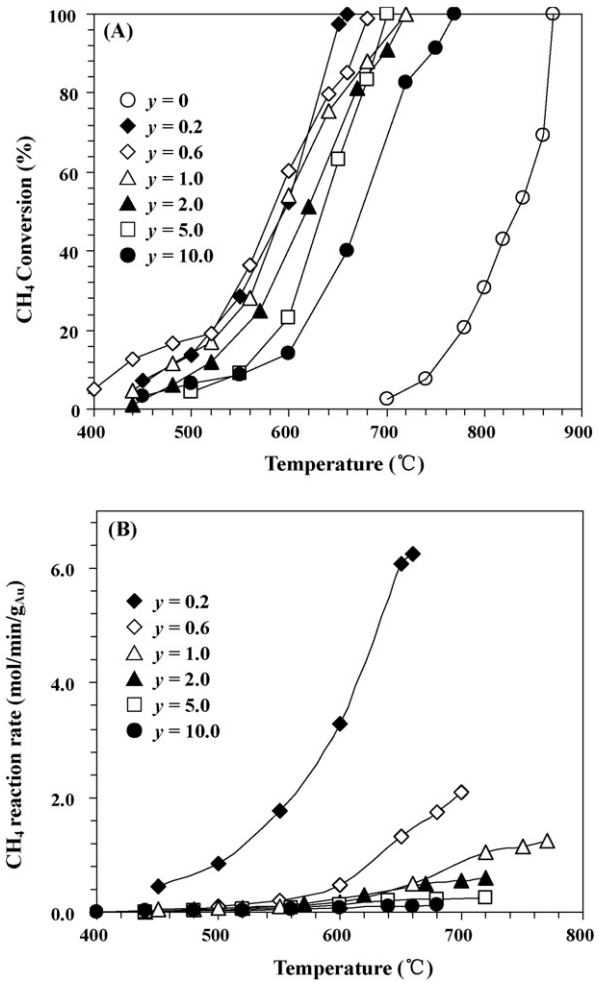

Fig. 6. (A) Methane conversion and (B) reaction rate versus temperature over the *y*% AuO_x/CZY catalysts at CH_4/O_2 molar ratio = 1/4 and space velocity = 50,000 h^{-1}.

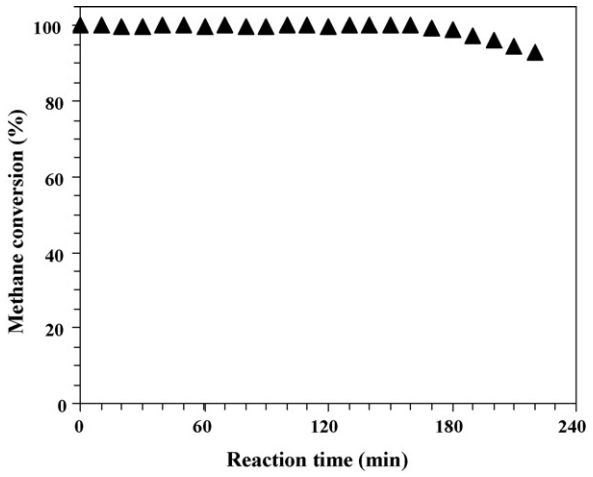

Fig. 7. Catalytic activity versus on-stream reaction time over 0.2% AuO_x/CZY for methane oxidation under the conditions of temperature = 660 °C, CH_4/O_2 molar ratio = 1/4, and space velocity = 50,000 h^{-1}.

that the 0.2% AuO_x/CZY catalyst performed much better than the Au/Al_2O_3 and $Au/MO_x/Al_2O_3$ (M = Co, Mn, Fe) catalysts ($T_{100\%} > 700$ °C at 1800 h^{-1}) for the oxidation of methane [41,42].

In Al_2O_3-supported PdO catalysts for methane combustion, there is generally presence of a hysteresis loop of catalytic activity versus temperature when the activities are measured by raising and decreasing the reaction temperature [1]. It is induced by the change of active phase composition from more active PdO to less active Pd^0 during the rise and drop in temperature. We also examined the effect of temperature rise and drop on the catalytic activities of *y*% AuO_x/CZY and the results are shown in Fig. 8. It is observed that the hysteresis loop of activity versus temperature appeared over the six catalysts, with the ones at *y* = 0.2 and 0.6 being minimized. We deduce that such phenomena were caused due to the partial reduction of the more active AuO_x to less active

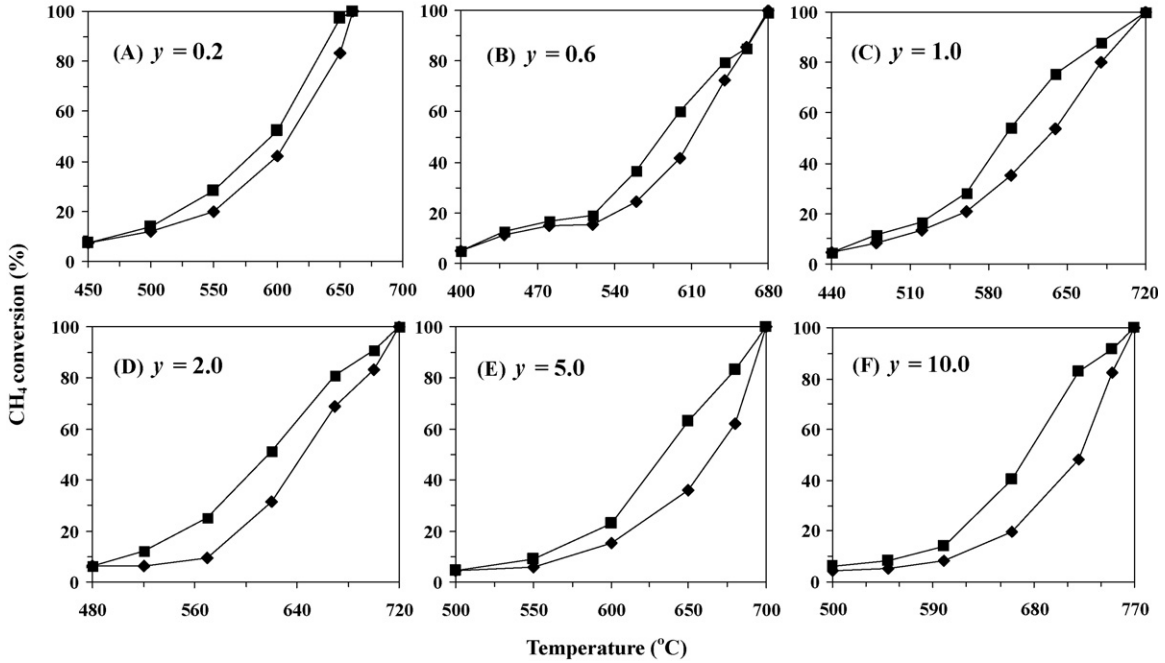

Fig. 8. Catalytic activities of *y*% AuO_x/CZY determined when the reaction temperature was increased (■) and decreased (◆) under the conditions of CH_4/O_2 molar ratio = 1/4 and space velocity = 50,000 h^{-1}.

Au^0 (as confirmed by the XPS result of the used 0.2% AuO_x/CZY catalyst) as well as the Ce^{4+} in CZY to Ce^{3+} at high temperatures, resulting in a decrease in activity determined during the period of temperature drop.

Corma and co-workers reported that there was a cooperation (i.e. synergistic action) between nano-sized gold and nanocrystalline CeO_{2-x} which promoted the formation of reactive oxygen (peroxide and superoxide) species at one electron defect sites [11]. The nanocrystalline CZY possessed a structure similar to and an oxygen vacancy density higher than nanocrystalline CeO_{2-x}. Therefore, we think that the good catalytic performance of AuO_x/CZY might be due to the stabilization of cationic gold [5,10] and reactive peroxide and superoxide species at the gold nanocluster–CZY interface as well as at the oxygen vacancies of the nanocrystalline redox-active CZY support. After investigating the CeO_2-supported gold catalysts for methane combustion, Bera and Hegde attributed the enhancement in catalytic activity to the presence of Au^{3+} ions as well as Au^0 nanoparticles and the Au^{3+} ions might be stabilized via the formation of $Ce_{1-x}Au_xO_{2-\delta}$ solid solution [32]. Similar scenario could exist in the *y*% AuO_x/CZY catalysts. Based on the about results and discussion, we therefore conclude that (i) a lower gold loading (<1.0%) on CZY favors the total oxidation of methane and (ii) the good catalytic performance of CZY-supported gold materials is related to the AuO_x dispersion, Au^{3+}/Au^0 atomic ratio, Au and CZY particle sizes, and reducibility.

4. Conclusions

The nanometer polycrystalline $Ce_{0.6}Zr_{0.3}Y_{0.1}O_2$ (CZY) support and its supported gold catalysts (*y*% AuO_x/CZY, *y*% represents the Au weight percentage, *y* = 0.2–10.0) could be fabricated using the CTAB-assisted hydrothermal treatment and *in situ* reduction methods (with $HAuCl_4$ as Au source, $NaBH_4$ as reducing agent, and PVP as surfactant), respectively. The characterization results showed that the CZY and gold were nano-sized particles with the respective diameter being ranged from 5 to 50 nm and from 2 to 20 nm; there was presence of highly dispersed AuO_x (Au^{3+}) domains on the CZY surfaces at the gold loading ≤0.6%, whereas above this loading the gold mainly existed in the form of metallic Au^0 cluster as well as dispersed AuO_x domains. The loading of gold markedly increased the reducibility of CZY, possibly due to the synergistic action between the nano-sized gold and the nanocrystalline CZY. Among the catalysts investigated in the present work, the 0.2% AuO_x/CZY one performed the best for the combustion of methane. We conclude that the AuO_x dispersion, Au^{3+}/Au^0 molar ratio, Au and CZY particle sizes, and catalyst reducibility are the factors influencing the catalytic performance of the CZY-supported gold materials.

Acknowledgments

This work was supported by the Project (Guo-Ren-Bu-Fa [2004] 99) and Jing-Ren-Fa [2004] 111), the PHR (IHLB) of Beijing Municipality, the SRF for ROCS (State Education Ministry of China), the Doctoral Scientific Research Initiation Foundation of Beijing University of Technology (KZ0502200301), and the Key Project of Natural Science Foundation of Beijing Municipality (3061001).

References

[1] D. Ciuparu, M.R. Lyubovsky, E. Altman, L.D. Pfefferle, A. Datye, Catal. Rev. 44 (2002) 593.
[2] M. Haruta, Catal. Today 110 (1997) 123.
[3] R.D. Waters, J.J. Weimer, J.E. Smith, Catal. Lett. 30 (1995) 181.
[4] E.D. Park, J.S. Lee, J. Catal. 186 (1999) 1.
[5] J. Guzman, B.C. Gates, J. Am. Chem. Soc. 126 (2004) 2672.
[6] G.J. Hutchings, M.S. Hall, A.F. Carley, P. Landon, B.E. Solsona, C.J. Kiely, A. Herzing, M. Makkee, J.A. Moulijn, A. Overweg, J.C. Fierro-Gonzalez, B.C. Gates, J. Catal. 242 (2006) 71.
[7] G.C. Bond, D.T. Thompson, Gold Bull. 33 (2000) 41.
[8] H.H. Kung, M.C. Kung, C.K. Costello, J. Catal. 216 (2003) 425.
[9] X. Zhang, H. Wang, B.Q. Xu, J. Phys. Chem. B 109 (2005) 9678.
[10] S. Carrettin, P. Concepción, A. Corma, J.L. Nieto, V.F. Puntes, Angew. Chem. Int. Ed. 43 (2004) 2538.
[11] J. Guzman, S. Carrettin, J.C. Fierro-Gonzalez, Y. Hao, B.C. Gates, A. Corma, Angew. Chem. Int. Ed. 44 (2005) 4778.
[12] H. He, H.X. Dai, K.W. Wong, C.T. Au, Appl. Catal., A 251 (2003) 61.
[13] S. Larrondo, M.A. Vidal, B. Irigoyen, A.F. Craievich, D.G. Lamas, I.O. Fábregas, G.E. Lascalea, N.E.W. de Reca, N. Amadeo, Catal. Today 107–108 (2005) 53.
[14] G.Z. Wang, L. Zhang, J.G. Deng, H.X. Dai, H. He, X.H. Zi, Chin. Sci. Bull. 52 (2007) 175.
[15] P.X. Huang, F. Wu, B.L. Zhu, X.P. Gao, H.Y. Zhu, T.Y. Yan, W.P. Huang, S.H. Wu, D.Y. Song, J. Phys. Chem. B 109 (2005) 19169.
[16] R.Z. Ma, T. Sasaki, Y. Bando, J. Am. Chem. Soc. 126 (2004) 10382.
[17] J.G. Huang, T. Kunitake, S.Y. Onoue, Chem. Commun. (2004) 1008.
[18] S.J. Gregg, Colloids Surf. 21 (1986) 109.
[19] A. Galtayries, R. Sporken, J. Riga, G. Blanchard, R. Caudano, J. Electron Spectrosc. Relat. Phenom. 88–91 (1998) 951–956.
[20] L. Zhu, J.J. Yu, X.Z. Wang, J. Hazard. Mater. 140 (2007) 205.
[21] G. Balducci, J. Kašpar, P. Fornasiero, M. Graziani, M.S. Islam, J.D. Gale, J. Phys. Chem. B 101 (1997) 1750.
[22] A. Martínez-Arias, M. Fernández-García, C. Belver, J.C. Conesa, J. Soria, Catal. Lett. 65 (2000) 197.
[23] Y. Madier, C. Descorme, A.M. Le Govic, D. Duprez, J. Phys. Chem. B 103 (1999) 10999.
[24] R. Si, Y.W. Zhang, L.M. Wang, S.J. Li, B.X. Lin, W.S. Chu, Z.Y. Wu, C.H. Yan, J. Phys. Chem. C 211 (2007) 787.
[25] E. Wuilloud, B. Delley, W.D. Schneide, Y. Baer, Phys. Rev. Lett. 53 (1984) 202.
[26] C. Ho, J.C. Yu, T. Kwong, A.C. Mak, S. Lai, Chem. Mater. 17 (2005) 4514.
[27] L.S. Zhong, J.S. Hu, A.M. Cao, Q. Liu, W.G. Song, L.J. Wan, Chem. Mater. 19 (2007) 1648.
[28] H. Vidal, J. Kašpar, M. Pijolat, G. Colonb, S. Bernal, A. Cordón, V. Perrichon, F. Fally, Appl. Catal. B 27 (2000) 49.
[29] H. He, H.X. Dai, L.H. Ng, K.W. Wong, C.T. Au, J. Catal. 206 (2002) 1.
[30] X. Zhang, H. Shi, B.Q. Xu, Catal. Today 122 (2007) 330.
[31] X. Zhang, H. Shi, B.Q. Xu, Angew. Chem. Int. Ed. 44 (2005) 7132.
[32] P. Bera, M.S. Hegde, Catal. Lett. 79 (2002) 75.
[33] E.D. Park, J.S. Lee, J. Catal. 186 (1996) 1.
[34] S. Schimpf, M. Lucas, C. Mohr, U. Rodemerck, A. Brückner, J. Radnic, H. Hofmeister, P. Claus, Catal. Today 72 (2002) 63.
[35] N.A. Hodge, C.J. Kiely, R. Whymanb, M.R.H. Siddiqui, G.J. Hutchings, Q.A. Pankhurst, F.E. Wagner, R.R. Rajaram, S.E. Golunski, Catal. Today 72 (2002) 133.
[36] M.P. Casaletto, A. Longo, A. Martorana, A. Prestianni, A.M. Venezia, Surf. Interface Anal. 38 (2006) 215.
[37] G. Jacobs, U.M.G. raham, E. Chenu, P.M. Patterson, A. Dozier, B.H. Davis, J. Catal. 229 (2005) 499.
[38] C. Milone, M. Fazio, A. Pistone, S. Galvagno, Appl. Catal. B 68 (2006) 28.
[39] S. Goulunski, R. Rajatam, N. Hodge, G.H. Hutchings, G.J. Kiely, Catal. Today 72 (2002) 107.
[40] A.A. Fonseca, J.M. Fisher, D. Ozkaya, M.D. Shannon, D. Thompsett, Top. Catal. 44 (2007) 223.
[41] R.J.H. Grisel, B.E. Nieuwenhuys, Catal. Today 64 (2001) 69.
[42] A.C. Gluhoi, B.E. Nieuwenhuys, Catal. Today 119 (2007) 305.